NANO LETTERS

Letter

pubs.acs.org/NanoLett

Direct Four-Probe Measurement of Grain-Boundary Resistivity and Mobility in Millimeter-Sized Graphene

Ruisong Ma,[†,‡] Qing Huan,[†] Liangmei Wu,[†,‡] Jiahao Yan,[†,‡] Wei Guo,[§] Yu-Yang Zhang,[†] Shuai Wang,[§] Lihong Bao,*[,†,‡] Yunqi Liu,[∥] Shixuan Du,[†,‡] Sokrates T. Pantelides,[⊥,†] and Hong-Jun Gao*[,†,‡]

[†]Institute of Physics & University of Chinese Academy of Sciences, Chinese Academy of Sciences, P.O. Box 603, Beijing 100190, People's Republic of China

[‡]Beijing Key Laboratory for Nanomaterials and Nanodevices, Beijing 100190, People's Republic of China

[§]School of Chemistry and Chemical Engineering, Huazhong University of Science and Technology, Wuhan 430074, People's Republic of China

[∥]Beijing National Laboratory for Molecular Sciences, Key Laboratory of Organic Solids, Institute of Chemistry, Chinese Academy of Science, Beijing 100190, People's Republic of China

[⊥]Department of Physics and Astronomy and Department of Electrical Engineering and Computer Science, Vanderbilt University, Nashville, Tennessee 37235, United States

S *Supporting Information*

ABSTRACT: Grain boundaries (GBs) in polycrystalline graphene scatter charge carriers, which reduces carrier mobility and limits graphene applications in high-speed electronics. Here we report the extraction of the resistivity of GBs and the effect of GBs on carrier mobility by direct four-probe measurements on millimeter-sized graphene bicrystals grown by chemical vapor deposition (CVD). To extract the GB resistivity and carrier mobility from direct four-probe intragrain and intergrain measurements, an electronically equivalent extended 2D GB region is defined based on Ohm's law. Measurements on seven representative GBs find that the maximum resistivities are in the range of several kΩ·μm to more than 100 kΩ·μm. Furthermore, the mobility in these defective regions is reduced to 0.4−5.9‰ of the mobility of single-crystal, pristine graphene. Similarly, the effect of wrinkles on carrier transport can also be derived. The present approach provides a reliable way to directly probe charge-carrier scattering at GBs and can be further applied to evaluate the GB effect of other two-dimensional polycrystalline materials, such as transition-metal dichalcogenides (TMDCs).

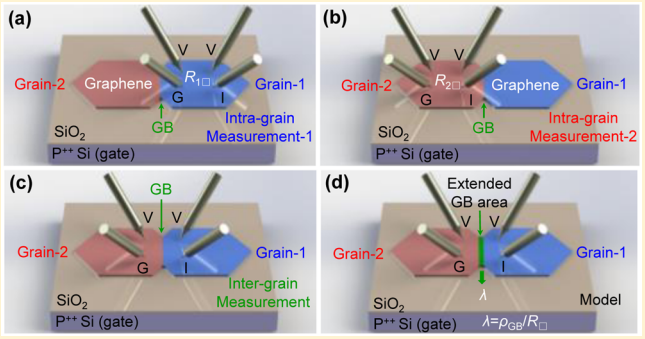

KEYWORDS: *Graphene, grain boundary, wrinkle, four-probe measurement, mobility*

Graphene's extraordinary mechanical, optical, and electrical properties[1−3] make it an emerging material for a wide range of applications, including field-effect transistors (FETs),[4] flexible and transparent electrodes,[5] and chemical/biochemical sensors.[6] However, an obstacle in practical electronic applications of large-area graphene is its polycrystalline nature and the presence of defects such as grain boundaries (GBs) and wrinkles in as-synthesized graphene by chemical vapor deposition (CVD). As topological line defects, graphene GBs consist of nonhexagonal carbon rings (pentagons, heptagons, and octagons), which have been imaged by scanning tunneling microscopy (STM),[7] scanning tunneling spectroscopy (STS),[8] and high-resolution transmission electron microscopy (HRTEM).[9,10] The electronic structure of pristine graphene is strongly perturbed near GBs,[11] whereby an "electronic transition width" ∼10 nm compared to the geometric width of GB (<1 nm) has been revealed by STM/STS[7,8,12,13] and scanning tunneling potentiometry (STP).[14] When charge carriers transport through the GBs, they undergo strong scattering and the mobility is reduced.[10,15−17] Therefore, quantitative characterization of charge-carrier transport across such topological defects by measuring their resistivity and carrier mobility would facilitate large-scale technological applications, such as touch-screen panels[5,18] and solar-cell electrodes.[19−21]

Previous investigations of electronic transport across graphene GBs have been performed by conventional four-terminal measurements, in which the resistances of the pristine grains on both sides and that of crossing the GB are measured on Hall bar structures fabricated by microfabrication

Received: April 18, 2017
Revised: July 13, 2017
Published: August 8, 2017

DOI: 10.1021/acs.nanolett.7b01624
Nano Lett. 2017, 17, 5291−5296

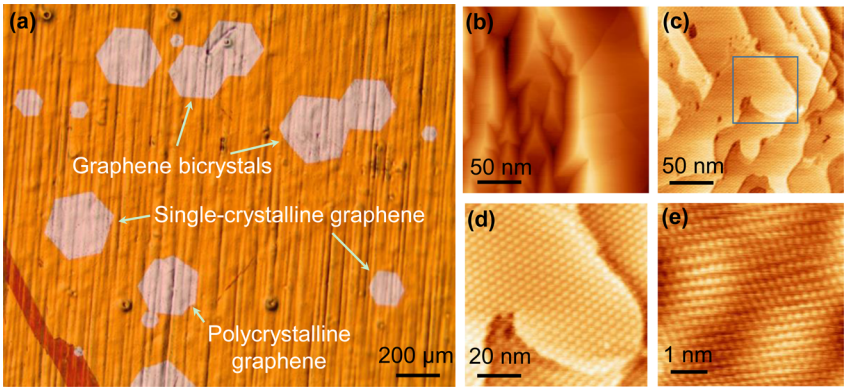

Figure 1. Optical and STM characterization of graphene grown on Cu foil by CVD. (a) Optical micrograph of graphene on a Cu foil substrate. Single-crystal, bicrystal and polycrystalline graphene flakes can be found on this micrograph. (b–c) Large-area STM image of graphene on Cu foil. The morphology of the Cu foil substrate is clearly resolved. (d) High-magnification STM image of the selected square region in (c). Hexagonal moiré pattern confirms the continuity of the graphene membrane on Cu substrate. (e) Atomically resolved STM image of the moiré pattern. These STM images verify the continuity and high quality of the graphene samples. Imaging parameters: (b) I_t = 250 pA and V_{sample} = 118.6 mV. (c) I_t = 358.6 pA and V_{sample} = 87.16 mV. (d) I_t = 600 pA and V_{sample} = 87.16 mV. (e) I_t = 800 pA and V_{sample} = 87.16 mV.

technique.[15,17] Taking the geometry factor into consideration, the intragrain resistivity and GB resistivity can be derived.[6,15−17,22] Scanning probe microscope (SPM) related techniques are also employed to investigate the transport properties of GBs, such as STP,[14] alternating current electrostatic force microscopy (AC-EFM)[9] and Kelvin probe force microscopy (KPFM).[23] Direct four-probe measurements on millimeter-sized graphene without Hall bar device fabrication have not yet been demonstrated.

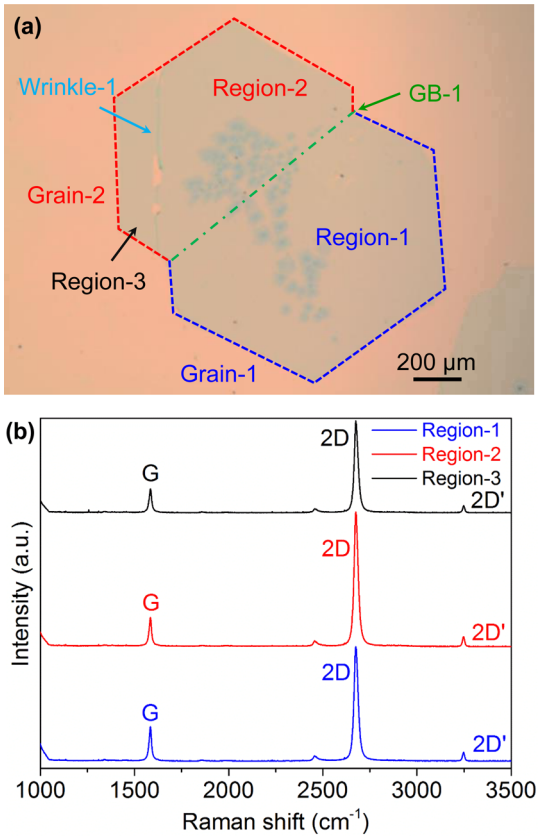

Figure 2. Optical and Raman characterization of monolayer graphene on SiO_2/Si substrate. (a) Optical micrograph of a monolayer graphene bicrystal containing grain-1 and grain-2 whose edges are indicated by blue and red dashed lines, respectively. The two grains are separated by a grain boundary (GB) denoted by a dark green dot-dash line. The graphene wrinkle is indicated by a light blue arrow on grain-2. (b) Raman spectra collected from the regions 1 to 3 of the monolayer graphene in (a) with an excitation wavelength of 532 nm of the laser. The spectra are offset vertically for clarity.

In this paper, we report direct four-probe measurements on millimeter-sized graphene on a SiO_2/Si substrate in a UHV four-probe STM system.[24] On the basis of Ohm's law, the effect of a GB on transport can be effectively considered as the additional resistance contribution from an extended 2D area. This extended area shares the same resistivity as the pristine graphene grain and its extent can be represented by a parameter λ.[17,22] By subtracting the intragrain contributions from the intergrain measurement, the parameter λ and GB resistivity can be obtained. Furthermore, the mobility in the GB region can also be derived. Our method is performed directly on the graphene grains without preliminary lithographic fabrication and thus retains the original features and properties of graphene. It can also be further extended to measure the GB effect in other 2D materials.

Millimeter-sized graphene samples were grown on Cu foil and then transferred onto a SiO_2/Si wafer (see Methods section in Supporting Information).[25] The graphene flakes can be found on Cu foil after CVD growth, as shown in the optical micrograph in Figure 1a. We see hexagonal islands that are identified as single-crystal graphene. Direct TEM evidence has been reported for similar samples in ref 10. Some of the hexagonal islands clearly form bicrystals. Nonhexagonal islands, on the other hand, are polycrystalline. We have carried out transport measurements only on bicrystals, ensuring that we measure single GBs. STM characterization has been performed to verify the continuity and quality of graphene on Cu foil. Two typical structures are shown in Figure 1b,c. Other morphologies are shown in Supporting Information Figure S1. As can be seen from these STM images, the Cu foil has a highly corrugated surface consisting of many irregular steps and even small pits. Figure 1d clearly reveals moiré patterns, formed by the lattice mismatch of the graphene layer with the underlying Cu foil surface. The uniform orientation of the moiré pattern across neighboring terraces of copper confirms the continuity of the graphene flake. The atomically resolved STM image of the

DOI: 10.1021/acs.nanolett.7b01624
Nano Lett. 2017, 17, 5291−5296

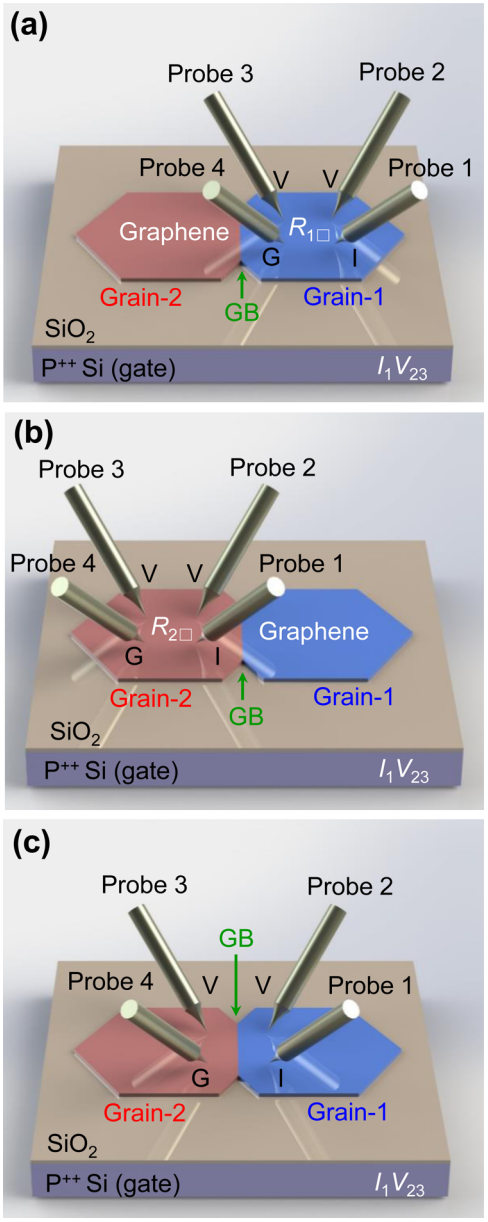

Figure 3. Schematic diagrams of four-probe measurements. (a,b) Four-probe measurements on the right grain (grain-1, blue) and the left grain (grain-2, red) of a graphene bicrystal on SiO_2/Si substrate, respectively. The GB is indicated by the dark green arrow. The sheet resistances of grain-1 and grain-2 are denoted as $R_1\square$ and $R_2\square$, respectively. (c) Four-probe measurement crossing GB. The grain-1 and grain-2 coalesce at the GB indicated by the dark green arrow. The four probes are labeled as probe 1 to 4. "*I*" indicates current injection while "*G*" means ground. "*V*" stands for voltage. The size in these drawings is not to scale.

moiré pattern shown in Figure 1e further verifies the continuity and high quality of the CVD-grown graphene on Cu foil. Atomically resolved STM images on the structures shown in Supporting Information Figure S1 also confirm that defect-free graphene is grown continuously as a single domain (Supporting Information Figure S2).

An optical micrograph of a transferred monolayer graphene bicrystal onto SiO_2/Si substrate is shown in Figure 2a in which the optical contrast verifies its monolayer nature.[4,26] This millimeter-sized flake contains two coalesced graphene grains whose edges are indicated by blue (grain-1) and red (grain-2) dashed lines, respectively. These two grains show nearly zero rotation angle, and the expected GB line can be revealed by connecting the joint points of the two graphene domains on the edge,[10] denoted by a dark green dot dash line in Figure 2a. A graphene wrinkle on grain-2 is also indicated by a light blue arrow. Raman spectra of the graphene flake are collected at three different regions (shown in Figure 2a) with an excitation wavelength of 532 nm of the laser, as presented in Figure 2b. The relative intensity ratio of the 2D and G peaks (>2:1) confirms the monolayer nature of this graphene bicrystal and the absence of the D peak confirms the high quality of the flake after transferred onto the SiO_2/Si substrate.[27]

In the direct four-probe measurements, the extremely sharp STM probes as electrodes contact the sample in a noninvasive way.[28,29] Figure 3a,b schematically shows the direct four-probe measurements on the right grain (blue, grain-1) and left grain (red, grain-2) of a graphene bicrystal, respectively. The 300 nm SiO_2 layer acts as a dielectric while the highly doped Si (P^{++} Si) layer below serves as gate electrode, by which the carrier densities of graphene can be tuned.[30] Similarly, a direct four-probe measurement crossing the GB can be performed as shown in Figure 3c. In the intragrain and intergrain measurements where the four STM probes denoted as 1−4 are forming a square, testing configuration I_1V_{23} is defined as follows. Probe 1 injects the current (I_1), probe 4 is grounded (G), while probes 2 and 3 are used to measure the potential difference V_{23} ($V_2 - V_3$) between them. The sheet resistances can be obtained after multiplying R_{I1V23} (V_{23}/I_1) by the geometry factor ($\sim 2\pi/\ln 2$), which is determined according to the spacing between the four probes (the detailed derivation is described in Supporting Information).

Figure 4a shows the sheet resistances of grain-1 ($R_{1\square}$, blue), grain-2 ($R_{2\square}$, red), and intergrain ($R_{\text{intergrain}\square}$, black) as a function of carrier densities derived from intragrain and intergrain measurements. The inset in Figure 4a shows the optical micrograph of four-probe measurement across GB-1. The consistency between intragrain sheet resistances $R_{1\square}$ and $R_{2\square}$ indicates the homogeneous nature of the graphene bicrystal at non-grain boundary regions. Therefore, we approximately consider $R_{1\square} \approx R_{2\square} = R_\square$ in the case of GB-1. Because of the presence of GB between grain-1 and grain-2, the intergrain sheet resistances $R_{\text{intergrain}\square}$ are apparently larger than those of intragrain $R_\square$, especially at high-carrier densities far away from the neutral point. In Hall bar device measurement,[6,15−17,22] all the electrons transport through the GB perpendicularly. By directly subtracting the intragrain sheet resistance $R_\square$ from intergrain sheet resistance $R_{\text{intergrain}\square}$, the resistivity of GB, ρ_{GB}, can be extracted.[6,15−17,22] Nevertheless, in our case the current injected by the current probes diffuses radially to all directions as schematically shown in Figure S4 (Supporting Information). As a result, the intragrain and intergrain sheet resistances, and the GB resistivity cannot be simply expressed in a linear relationship.

In the present four-probe case, if the GB coincides exactly with the symmetry axis of the square formed by the four probes, the current passes through the GB almost without a parallel component, as in the case of the device measurements.[15,17] Therefore, the GB can be considered an extension of the conductance channel along the GB's normal. In order to extract the GB resistivity, the 1D GB is transformed into an extended 2D area as in ref 17 and this extended 2D area can be characterized by a parameter λ

DOI: 10.1021/acs.nanolett.7b01624
Nano Lett. 2017, 17, 5291−5296

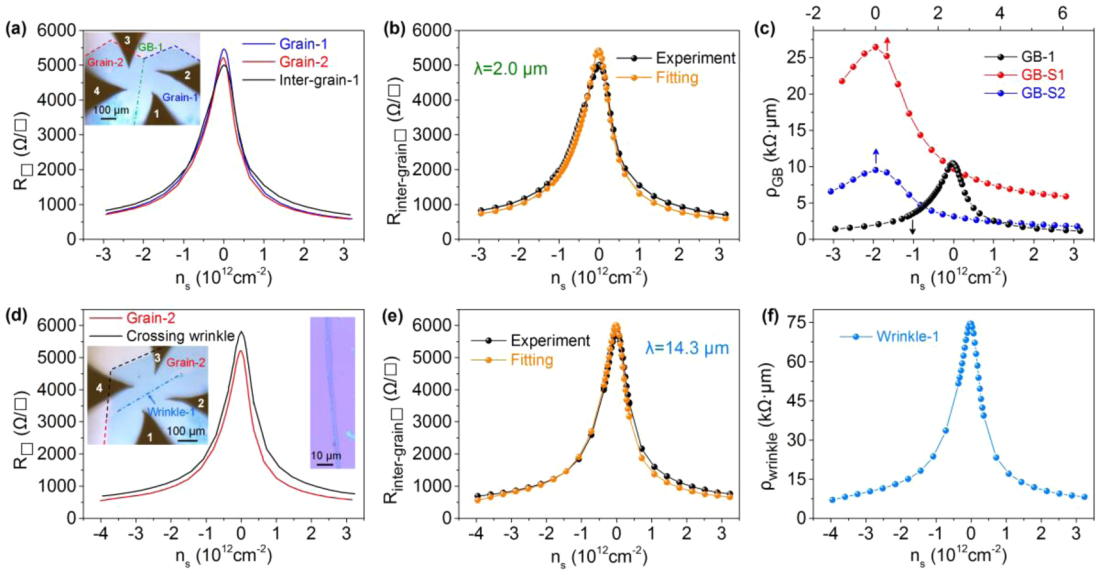

Figure 4. Four-probe measurement across the GB-1 and wrinkle. (a) Intragrain (blue for grain-1 and red for grain-2) and intergrain (black, crossing GB-1) sheet resistances as a function of carrier densities. The inset shows the optical micrograph of four-probe measurement crossing GB-1. (b) Comparison of experimental (black) and fitting data (orange) at different carrier densities. (c) Extracted resistivity of GB-1 (black), GB-S1 (red), and GB-S2 (blue) under a series of carrier densities. (d) Sheet resistance on grain-2 (red) and across the graphene wrinkle-1 (black). The inset on the left shows the optical micrograph of the four-probe measurement crossing the winkle while the right inset shows a magnified optical image of the wrinkle. (e) Experimental data (black) and calculated result (orange) according to our model. (f) The extracted wrinkle resistivity based on the model.

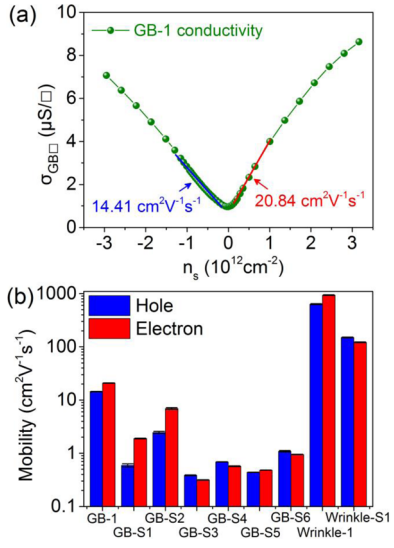

Figure 5. Mobility extraction for GB-1 and summary of mobility for GBs and wrinkles. (a) Electrical conductivity of GB-1 as a function of carrier densities. The hole and electron mobility are extracted by linearly fitting the conductivity curves indicated by the blue and red lines, respectively. (b) Summary of extracted hole and electron mobility values for GBs and wrinkles. The error bars are also shown in this histogram.

$$\lambda = \frac{\rho_{GB}}{R_{\square}} \tag{1}$$

where ρ_{GB} is defined as the GB resistivity (in unit kΩ·μm) and $R_{\square}$ (in unit Ω/□) is the intragrain sheet resistance (see Supporting Information Figure S3). In this way, the sheet resistance in the extended area (dark green area with an effective extent λ), indicated by a dark green arrow in Figure S3, is by definition the same as the sheet resistance of a pristine graphene grain ($R_{\square}$). In contrast with the linear relationship in the device method,[17] the relation between λ, $R_{\square}$, and intergrain sheet resistance $R_{\text{intergrain}\square}$ in our four-probe measurement is expressed by

$$R_{\text{intergrain}\square} = f(R_{\square}, s, \lambda) = \frac{R_{\square}}{\ln 2}\ln\left(\frac{s^2 + (s+\lambda)^2}{s^2}\right) \tag{2}$$

where s is the side length of the square formed by the four probes (a detailed derivation is given in Supporting Information). Since $R_{\text{intergrain}\square}$, s, and $R_{\square}$ can be easily obtained and only λ is unknown, the parameter λ can be obtained by solving eq 2 directly. The GB resistivity ρ_{GB} can then be extracted from eq 1.

Tsen et al. reported that the parameter λ is approximately a constant and independent of carrier densities.[17] The observed small variations of λ suggest that λ can be considered to be a constant for all carrier densities as well (Supporting Information Figure S6). As shown in Figure 4b, fitting the experimental data with eqs 1 and 2, λ = 2.0 μm is obtained. This value of λ is the same order of magnitude as found in ref 17. According to eq 1, the GB resistivity ρ_{GB} under different carrier densities can be extracted (as shown in Figure 4c). We find ρ_{GB} for GB-1 at the neutral point is 10.5 kΩ·μm. Measurements on other two GBs (GB-S1, GB-S2 in Supporting Information Figure S7) show that the maximum GB resistivities are 26.4 and 9.5 kΩ·μm for GB-S1 and GB-S2, respectively (as shown in Figure 4c). Experiment and fitting results of another four GBs (labeled as GB-S3, GB-S4, GB-S5, and GB-S6) can be found in Supporting Information Figures S9–S12. Our data for the graphene GB resistivity agree well with previous reports, in which the extracted GB resistivity from device measurements is in the range of ∼1 to 100 kΩ·μm.[22]

The large deviations of GB resistivity in the seven different GBs may originate from two aspects. First, these GBs are

DOI: 10.1021/acs.nanolett.7b01624
Nano Lett. 2017, 17, 5291−5296

Table 1. Summary of the Hole and Electron Mobility with Error, Transition Width W, Effective Extent λ, and W/λ for All the Line Defects

name	hole mobility ($cm^2\ V^{-1}\ s^{-1}$)	electron mobility ($cm^2\ V^{-1}\ s^{-1}$)	W	λ	W/λ
GB-1	14.41 ± 0.17	20.84 ± 0.26	10 nm	2.0 μm	0.50%
GB-S1	0.5887 ± 0.0424	1.892 ± 0.036	10 nm	4.6 μm	0.22%
GB-S2	2.453 ± 0.132	6.917 ± 0.280	10 nm	1.7 μm	0.59%
GB-S3	0.3870 ± 0.0075	0.3148 ± 0.0042	10 nm	28.8 μm	0.04%
GB-S4	0.6887 ± 0.0071	0.5722 ± 0.0077	10 nm	14.3 μm	0.07%
GB-S5	0.4374 ± 0.0037	0.4809 ± 0.0014	10 nm	19.7 μm	0.05%
GB-S6	1.091 ± 0.0370	0.947 ± 0.0125	10 nm	10.0 μm	0.10%
wrinkle-1	634.8 ± 11.3	935.5 ± 15.5	3.3 μm	14.3 μm	23.10%
wrinkle-S1	150.1 ± 2.9	121.9 ± 2.5	3.0 μm	17.9 μm	16.60%

formed when pristine graphene domains are stitched together to generate a larger domain during growth and better intergrain connectivity would lead to lower GB resistivity.[17] Therefore, the difference in intergrain connectivity can result in the deviations of GB resistivity. Second, the difference may come from functional groups or adsorbates, which preferentially attach to these defective GBs[8] and can effectively change the GB resistivity.[6,22] The difference in content and variety of the residual attachment after vacuum annealing also gives rise to the deviations of GB resistivity.

The wrinkle resistivity can also be extracted through similar measurements for GB, as shown in the inset of Figure 4d. The intragrain (pristine, red) and intergrain (crossing wrinkle, black) sheet resistances as a function of carrier densities are shown in Figure 4d. The sheet resistance crossing wrinkle-1 is apparently larger than that of pristine graphene, indicating the additional resistance contribution from a wrinkle when carriers transport through it. Fitting the experimental data with eqs 1 and 2, λ = 14.3 μm can be obtained. The wrinkle resistivity at neutral point is 74.5 k$\Omega\cdot\mu$m as shown in Figure 4f. By the same method, the effective parameter λ and maximum wrinkle resistivity of wrinkle-S1 are 17.9 μm and 146.2 k$\Omega\cdot\mu$m (Supporting Information Figure S13).

The presence of GBs would alter the electronic structure near the GB region over a scale ~10 nm as verified by STM, STS, and STP.[8,12−14] An STM image of a graphene GB on Cu foil is shown in Figure S15a (Supporting Information). The width W of this GB is approximately 10 nm, as revealed by the line profile shown in Figure S10b (Supporting Information). According to previous STS studies, this electronic transition region, which is much wider in scale compared with the atomically sharp structural transition, arises from the doping concentration variation near the GB area.[8,14] Because the scattering at the electronic transition region leads to the additional resistance at GB, the mobility at the electronic transition region can be estimated from the GB resistivity. According to eq 1, the conductivity of the electronic transition region $\sigma_{GB\square}$ can be calculated by

$$\sigma_{GB\square} = \frac{1}{R_{GB\square}} = \frac{W}{\rho_{GB}} \tag{3}$$

in which $R_{GB\square}$ is the sheet resistance of the GB transition region whose width W is ~10 nm.

Accordingly, the conductivity of the electronic transition region at GB-1 under different carrier densities can be obtained, as shown in Figure 5a. By linearly fitting the conductivity curves, indicated by the blue and red lines, the hole and electron mobility of GB-1 are found to be 14.41 ± 0.17 and 20.84 ± 0.26 $cm^2\ V^{-1}\ s^{-1}$, respectively. For the graphene wrinkle, the hole and electron mobility in the wrinkle area are extracted as 634.8 ± 11.3 and 935.5 ± 15.5 $cm^2\ V^{-1}\ s^{-1}$, respectively. The mobility of the measured GBs and wrinkles are summarized in Figure 5b. GB-S3 shows the lowest mobility while wrinkle-1 possesses the greatest values. This suggests that the presence of nonhexagonal carbon rings would bring much higher resistance than just the folding of graphene layers.

The relation of mobility in the GB transition region and the intragrain (pristine) mobility satisfies (see details in Supporting Information)

$$\frac{\mu_{GB}}{\mu_{pristine}} = \frac{W}{\lambda} \tag{4}$$

On the basis of eq 4, for GB-1 λ = 2.0 μm and the estimated ratio of W to λ is equal to 0.50%. Table 1 summarizes the hole and electron mobility, transition width W, effective parameter λ, and ratio of them W/λ for all the line defects. As can be seen from this table, the W/λ values for the seven boundaries are all lower than 0.60%. These low ratios manifest that the structural defects like GBs serve as a source of strong intrinsic carrier scattering, which limits the carrier mobility of polycrystalline graphene. As for the graphene wrinkle-1 and wrinkle-S1, the averaged width is about 3.3 and 3.0 μm, respectively (Supporting Information), and their respective average ratios are ~23% and ~16.6%, much higher than that of a GB. This indicates that grain boundary induces stronger carrier scattering than that of wrinkle.

In conclusion, we demonstrate direct four-probe measurements of the resistivity and carrier mobility of GB/wrinkle in monolayer graphene on a SiO_2/Si substrate. To evaluate the effect of GB/wrinkle on electrical transport of graphene quantitatively, a model based on Ohm's law is proposed. Measurements on seven typical graphene GBs and two typical wrinkles suggest the feasibility of the model. The extracted GB/wrinkle resistivity is much higher and their carrier mobility is much lower than those of the pristine graphene, revealing the strong scattering effects for carriers at these defects. Moreover, grain boundaries show much stronger carrier scattering than wrinkles. Our method can be easily extended to measure other 2D materials like TMDCs with GBs and may shed light on the limiting factors of electronic devices.

■ ASSOCIATED CONTENT

Supporting Information

The Supporting Information is available free of charge on the ACS Publications website at DOI: 10.1021/acs.nanolett.7b01624.

DOI: 10.1021/acs.nanolett.7b01624
Nano Lett. 2017, 17, 5291−5296

CVD growth method of graphene on Cu foil and transfer technique, characterization method (Raman spectra, electrical transport measurement, STM and AFM imaging), extraction of intragrain and intergrain sheet resistance, extending the 1D GB defect into a 2D domain, derivation of the sheet resistance crossing the GB, converting the gate voltage to sheet carrier densities of graphene, extraction of hole and electron mobility for a 2D sample, ratio of mobility at GB electronic transition region with intragrain mobility, width of the graphene wrinkle (PDF)

AUTHOR INFORMATION

Corresponding Authors

*E-mail: lhbao@iphy.ac.cn.
*E-mail: hjgao@iphy.ac.cn.

ORCID

Yu-Yang Zhang: 0000-0002-9548-0021
Shuai Wang: 0000-0001-9328-0408
Lihong Bao: 0000-0002-2942-892X
Shixuan Du: 0000-0001-9323-1307
Hong-Jun Gao: 0000-0002-6766-0623

Notes

The authors declare no competing financial interest.

ACKNOWLEDGMENTS

This work is supported by National "973" Projects of China (Grant 2013CBA01600), National Key R&D Program of China (Grant 2016YFA0202300), National Natural Science Foundation of China (Grants 61474141, 61674170, 61335006, 61390501, 51325204, 51210003), the Chinese Academy of Sciences (CAS), the CAS Pioneer Hundred Talents Program, and Youth Innovation Promotion Association of CAS (20150005). Work at Vanderbilt University was supported by U.S. Department of Energy Grant DE-FG02-09ER46554 and by the McMinn Endowment. Y.Y.Z. and S.T.P. acknowledge National Center for Supercomputing Applications, which is supported by the DOE Office of Science under Contract No. DE-AC02-05CH11231, and the Extreme Science and Engineering Discovery Environment (XSEDE) which is supported by National Science Foundation Grant ACI-1053575.

REFERENCES

(1) Lee, C.; Wei, X. D.; Kysar, J. W.; Hone, J. *Science* **2008**, *321* (5887), 385−388.
(2) Morozov, S. V.; Novoselov, K. S.; Katsnelson, M. I.; Schedin, F.; Elias, D. C.; Jaszczak, J. A.; Geim, A. K. *Phys. Rev. Lett.* **2008**, *100* (1), 016602.
(3) Bonaccorso, F.; Sun, Z.; Hasan, T.; Ferrari, A. C. *Nat. Photonics* **2010**, *4* (9), 611−622.
(4) Novoselov, K. S.; Geim, A. K.; Morozov, S. V.; Jiang, D.; Zhang, Y.; Dubonos, S. V.; Grigorieva, I. V.; Firsov, A. A. *Science* **2004**, *306* (5696), 666−669.
(5) Bae, S.; Kim, H.; Lee, Y.; Xu, X. F.; Park, J.-S.; Zheng, Y.; Balakrishnan, J.; Lei, T.; Kim, H. R.; Song, Y. I.; Kim, Y.-J.; Kim, K. S.; Özyilmaz, B.; Ahn, J.-H.; Hong, B. H.; Iijima, S. *Nat. Nanotechnol.* **2010**, *5* (8), 574−578.
(6) Yasaei, P.; Kumar, B.; Hantehzadeh, R.; Kayyalha, M.; Baskin, A.; Repnin, N.; Wang, C.; Klie, R. F.; Chen, Y. P.; Král, P.; Salehi-Khojin, A. *Nat. Commun.* **2014**, *5*, 4911.
(7) Lahiri, J.; Lin, Y.; Bozkurt, P.; Oleynik, I. I.; Batzill, M. *Nat. Nanotechnol.* **2010**, *5* (5), 326−329.
(8) Tapasztó, L.; Nemes-Incze, P.; Dobrik, G.; Yoo, K. J.; Hwang, C.; Biró, L. P. *Appl. Phys. Lett.* **2012**, *100* (5), 053114.
(9) Huang, P. Y.; Ruiz-Vargas, C. S.; van der Zande, A. M.; Whitney, W. S.; Levendorf, M. P.; Kevek, J. W.; Garg, S.; Alden, J. S.; Hustedt, C. J.; Zhu, Y.; Park, J.; McEuen, P. L.; Muller, D. A. *Nature* **2011**, *469* (7330), 389−392.
(10) Guo, W.; Wu, B.; Li, Y.; Wang, L.; Chen, J.; Chen, B.; Zhang, Z.; Peng, L.; Wang, S.; Liu, Y. *ACS Nano* **2015**, *9* (6), 5792−5798.
(11) Castro Neto, A. H.; Guinea, F.; Peres, N. M. R.; Novoselov, K. S.; Geim, A. K. *Rev. Mod. Phys.* **2009**, *81* (1), 109−162.
(12) Nemes-Incze, P.; Vancsó, P.; Osváth, Z.; Márk, G. I.; Jin, X.; Kim, Y.-S.; Hwang, C.; Lambin, P.; Chapelier, C.; PéterBiró, L. *Carbon* **2013**, *64*, 178−186.
(13) Koepke, J. C.; Wood, J. D.; Estrada, D.; Ong, Z.-Y.; He, K. T.; Pop, E.; Lyding, J. W. *ACS Nano* **2013**, *7* (1), 75−86.
(14) Clark, K. W.; Zhang, X.-G.; Vlassiouk, I. V.; He, G. W.; Feenstra, R. M.; Li, A.-P. *ACS Nano* **2013**, *7* (9), 7956−7966.
(15) Yu, Q.; Jauregui, L. A.; Wu, W.; Colby, R.; Tian, J.; Su, Z.; Cao, H.; Liu, Z.; Pandey, D.; Wei, D.; Chung, T. F.; Peng, P.; Guisinger, N. P.; Stach, E. A.; Bao, J.; Pei, S.-S.; Chen, Y. P. *Nat. Mater.* **2011**, *10* (6), 443−449.
(16) Jauregui, L. A.; Cao, H. L.; Wu, W.; Yu, Q. K.; Chen, Y. P. *Solid State Commun.* **2011**, *151* (16), 1100−1104.
(17) Tsen, A. W.; Brown, L.; Levendorf, M. P.; Ghahari, F.; Huang, P. Y.; Havener, R. W.; Ruiz-Vargas, C. S.; Muller, D. A.; Kim, P.; Park, J. *Science* **2012**, *336* (6085), 1143−1146.
(18) Ryu, J.; Kim, Y.; Won, D.; Kim, N.; Park, J. S.; Lee, E.-K.; Cho, D.; Cho, S.-P.; Kim, S. J.; Ryu, G. H.; Shin, H. A. S.; Lee, Z.; Hong, B. H.; Cho, S. *ACS Nano* **2014**, *8* (1), 950−956.
(19) Wang, X.; Zhi, L.; Müllen, K. *Nano Lett.* **2008**, *8* (1), 323−327.
(20) Ahmad, M.; An, H.; Kim, Y. S.; Lee, J. H.; Jung, J.; Chun, S.-H.; Seo, Y. *Nanotechnology* **2012**, *23* (28), 285705.
(21) Wu, J.; Becerril, H. A.; Bao, Z.; Liu, Z.; Chen, Y.; Peumans, P. *Appl. Phys. Lett.* **2008**, *92* (26), 263302.
(22) Cummings, A. W.; Duong, D. L.; Nguyen, V. L.; Van Tuan, D.; Kotakoski, J.; Barrios Vargas, J. E.; Lee, Y. H.; Roche, S. *Adv. Mater.* **2014**, *26* (30), 5079−5094.
(23) Willke, P.; Mohle, C.; Sinterhauf, A.; Kotzott, T.; Yu, H. K.; Wodtke, A.; Wenderoth, M. *Carbon* **2016**, *102*, 470−476.
(24) Ma, R.; Huan, Q.; Wu, L.; Yan, J.; Zou, Q.; Wang, A.; Bobisch, C. A.; Bao, L.; Gao, H.-J. *Rev. Sci. Instrum.* **2017**, *88* (6), 063704.
(25) Guo, W.; Jing, F.; Xiao, J.; Zhou, C.; Lin, Y.; Wang, S. *Adv. Mater.* **2016**, *28* (16), 3152−3158.
(26) Blake, P.; Hill, E. W.; Neto, A. H. C.; Novoselov, K. S.; Jiang, D.; Yang, R.; Booth, T. J.; Geim, A. K. *Appl. Phys. Lett.* **2007**, *91* (6), 063124.
(27) Ferrari, A. C.; Meyer, J. C.; Scardaci, V.; Casiraghi, C.; Lazzeri, M.; Mauri, F.; Piscanec, S.; Jiang, D.; Novoselov, K. S.; Roth, S.; Geim, A. K. *Phys. Rev. Lett.* **2006**, *97* (18), 187401.
(28) Nakayama, T.; Kubo, O.; Shingaya, Y.; Higuchi, S.; Hasegawa, T.; Jiang, C.-S.; Okuda, T.; Kuwahara, Y.; Takami, K.; Aono, M. *Adv. Mater.* **2012**, *24* (13), 1675−1692.
(29) Lu, H. L.; Zhang, C. D.; Guo, H. M.; Gao, H. J.; Liu, M.; Liu, J.; Collins, G.; Chen, C. L. *ACS Appl. Mater. Interfaces* **2010**, *2* (9), 2496−2499.
(30) Dorgan, V. E.; Bae, M.-H.; Pop, E. *Appl. Phys. Lett.* **2010**, *97* (8), 082112.

DOI: 10.1021/acs.nanolett.7b01624
Nano Lett. 2017, 17, 5291−5296